MIT Open Access Articles

A phenomenological approach to modeling chemical dynamics in nonlinear and two-dimensional spectroscopy

The MIT Faculty has made this article openly available. ***Please share*** how this access benefits you. Your story matters.

Citation: Ramasesha, Krupa et al. "A Phenomenological Approach to Modeling Chemical Dynamics in Nonlinear and Two-dimensional Spectroscopy." The Journal of Chemical Physics 136.13 (2012): 134507. Web.

As Published: http://dx.doi.org/10.1063/1.3700718

Publisher: American Institute of Physics (AIP)

Persistent URL: http://hdl.handle.net/1721.1/73991

Version: Author's final manuscript: final author's manuscript post peer review, without publisher's formatting or copy editing

Terms of use: Creative Commons Attribution-Noncommercial-Share Alike 3.0

A phenomenological approach to modeling chemical dynamics in nonlinear and two-dimensional spectroscopy

Krupa Ramasesha, Luigi De Marco, Andrew D. Horning, Aritra Mandal and Andrei Tokmakoff*

Department of Chemistry, Massachusetts Institute of Technology, Cambridge, MA 02139 USA

Abstract

We present an approach for calculating nonlinear spectroscopic observables, which overcomes the approximations inherent to current phenomenological models without requiring the computational cost of performing molecular dynamics simulations. The trajectory mapping method uses the semi-classical approximation to linear and nonlinear response functions, and calculates spectra from trajectories of the system's transition frequencies and transition dipole moments. It rests on identifying dynamical variables important to the problem, treating the dynamics of these variables stochastically, and then generating correlated trajectories of spectroscopic quantities by mapping from the dynamical variables. This approach allows one to describe non-Gaussian dynamics, correlated dynamics between variables of the system, and nonlinear relationships between spectroscopic variables of the system and the bath such as non-Condon effects. We illustrate the approach by applying it to three examples that are often not adequately treated by existing analytical models – the non-Condon effect in the nonlinear infrared spectra of water, non-Gaussian dynamics inherent to strongly hydrogen bonded systems, and chemical exchange processes in barrier crossing reactions. The methods described are generally applicable to nonlinear spectroscopy throughout the optical, infrared and terahertz regions.

1. Introduction

Ultrafast spectroscopy is the most widely used experimental approach for studying the dynamics of molecules in condensed phases. The interpretation of these experiments has relied heavily on nonlinear spectroscopy models which use perturbation theory to describe the dynamics in terms of multi-point correlation functions in the dipole operator. The most useful models to have been embraced by experimentalist and theoretician alike provide the ability to directly calculate the measured experimental observables, allowing interpretation and fitting of the data. Unfortunately, in several cases, the assumptions built into these models are proving to be too restrictive to properly describe nonlinear and two-dimensional infrared spectroscopy. To provide a realistic interpretation of such data, mixed quantum-classical models that use classical molecular dynamics (MD) simulations to describe the dynamics are being widely developed. These models map the classical coordinates of the MD simulation onto a quantum Hamiltonian for the spectroscopic degrees of freedom and provide direct insight into how specific dynamics influence the spectroscopy. However, they usually add a layer of complexity that makes them impractical for experimentalists. The goal of this paper is to present a simple and intuitive approach to modeling nonlinear spectroscopy that describes the system and dynamics phenomenologically but calculates observables from trajectories and mapping variables as performed in mixed quantum-classical calculations.

The most popular approach to modeling nonlinear spectroscopy are the class of models that include the Brownian oscillator model and spin-boson model, which were popularized by Mukamel,[1] and are often implemented with the aid of double-sided Feynman diagrams. This method treats the interaction of one or more quantum degrees of freedom with a quantum harmonic bath.[1–4] Within that framework, it provides exact analytical expressions for observables in nonlinear spectroscopy, given variables that describe the system and the frequency correlation function or spectral density for the bath. The high temperature limit and specific forms of the bath lead to simple analytic descriptions of homogeneous and inhomogeneous broadening and spectral diffusion.

Analytical models typically rely on a series of approximations, including bilinear coupling of the system to a harmonic bath, the second cumulant approximation, and the Condon approximation. Perhaps the most restrictive is the use of the cumulant expansion to second order, also known as the Gaussian approximation. This allows the signal to be described exactly for Gaussian fluctuations or disorder in the system coordinate, which finds greatest use for the description of fluctuations about a free energy minimum. Barrier crossings, kinetics, and other non-Gaussian chemical dynamics are not accounted for, but are often added in an *ad hoc* manner. Bilinear coupling to a bath provides the ability to solve this problem analytically, but it only describes pure dephasing processes. Population relaxation and orientational relaxation must still be added in a manner that is uncorrelated with the pure dephasing. Finally, the Condon approximation states that the external electromagnetic field couples to a dipole operator that is a function of the system coordinates but not the bath. These approximations are proving to be too restrictive for many recent applications of nonlinear and two-dimensional infrared spectroscopy, which has spurred investigations into alternative methods of extracting such information from experiment.[5–7]

The past decade has also seen the growth of spectroscopic models based on the semi-classical approximation that draw from classical MD simulations. A number of variations for these mixed quantum-classical models exist, but they share in common a classical treatment of the molecular dynamics and the construction of a time-dependent quantum Hamiltonian for the spectroscopic degrees of freedom by mapping from one or more coordinates of the classical simulation.[8–12] These approaches may be used for spectroscopy of excitonic states and for reactive systems. They provide an atomistic interpretation of spectroscopic observables by nature of their direct correlation with underlying molecular dynamics. These advantages come at the cost of considerable effort for developing models and implementing the simulations, which makes them less accessible to experimentalists.

Existing models have proven very useful for many problems in nonlinear spectroscopy, and continue to be the favorite for the analysis of condensed phase dynamics. However, the advent of two-dimensional spectroscopy, and the growth of infrared vibrational spectroscopy in particular, has highlighted the need for a new class of models to analyze the spectroscopy of dynamics in complex and reactive systems. Previously, a few approaches to stochastically model vibrational dynamics using semi-classical methods have been put forth to describe linear[13] and nonlinear infrared spectroscopy.[14–17] Here we describe a phenomenological approach, which draws on the semi-classical approximation and can be used to describe the nonlinear spectroscopy of barrier crossings, non-Gaussian dynamics, and the non-Condon effect. It draws from mixed quantum-classical modeling, using stochastic trajectories for one or more system coordinates that are constructed in a phenomenological manner, and mapping variables that relate these internal coordinates to the spectroscopic observables. This trajectory mapping method provides an avenue to interpreting nonlinear and two-dimensional spectroscopy in the optical and infrared regimes in terms of known dynamics of internal coordinates.

2. Approach

a. Approximations to the Response Function

The common description of spectroscopy emerges from a Hamiltonian $H = H_0 + V(t)$ where H_0 is the Hamiltonian for the matter and $V(t) = -\mathbf{m} \cdot \mathbf{E}$ describes the electromagnetic field **E** interacting with the matter through the quantum mechanical dipole operator **m**.[1,18] Within linear response theory, time-domain spectroscopy depends on response functions, which are expressed as multipoint correlation functions in **m**. In the case of linear spectroscopy, the response function is related to $\langle \mathbf{m}(t) \cdot \mathbf{m}(0) \rangle$, and the time-evolution of the dipole moment **m**(t) for all degrees of freedom can be obtained directly from *ab initio* molecular dynamics simulations[19] or a classical representation of the dipole operator.[20] To reduce computational cost and complexity, one typically focuses only on the specific degrees of freedom that are resonant with **E**. This amounts to separating the spectroscopic degrees of freedom ("system" *Q*) from the remaining ones ("bath" *q*), which we account for by partitioning $H_0 = H_S + H_B + H_{SB}$, where H_{SB} describes the interaction between the "system" and the "bath". In the case of vibrational spectroscopy, one can expand **m** in *Q* and *q*. For instance, when including the permanent dipole, transition dipole moment, and linear non-Condon corrections to the transition dipole we have,

$$\mathbf{m} = \mathbf{m}_0 + \frac{\partial \mathbf{m}}{\partial Q} Q + \sum_{\alpha} \frac{\partial^2 \mathbf{m}}{\partial Q \partial q_\alpha} Q q_\alpha \tag{1}$$

Then, we can write dipole correlation functions in terms of the transition dipole moment $\bar{\mu}_{ab}(t) = \langle a | \mathbf{m}(t) | b \rangle$ where matrix elements are taken in the eigenstates of H_S, and the time dependence results from H_B. The linear response function for a two-level system with system states *a* and *b* becomes,

$$R^{(1)}(\tau) = \mathrm{Re}\left\langle \bar{\mu}_{ab}(\tau)\bar{\mu}_{ba}(0)\ \exp\left[-i\int_0^{\tau} \omega_{ba}(\tau')d\tau'\right]\right\rangle \tag{2}$$

Here the time-dependent transition energy $\omega_{ab}(t) = \left(\langle a|H_S + H_{SB}|a\rangle - \langle b|H_S + H_{SB}|b\rangle\right)/\hbar$, and the angular brackets denote a trace over the bath degrees of freedom. For nonlinear vibrational spectroscopy, the result for rephasing (–) and non-rephasing (+) contributions to the third-order response function is [4]

$$\begin{aligned} \mathrm{R}_{+}^{(3)} &= \sum_{\mathrm{abcd}} \left\langle \bar{\mu}_{\mathrm{ab}}(\tau_3+\tau_2+\tau_1)\bar{\mu}_{\mathrm{bc}}(\tau_2+\tau_1)\bar{\mu}_{\mathrm{cd}}(\tau_1)\bar{\mu}_{\mathrm{da}}(0)\mathrm{f}_{\mathrm{abcd}}^{(+)}\right\rangle \\ \mathrm{R}_{-}^{(3)} &= \sum_{\mathrm{abcd}} \left\langle \bar{\mu}_{\mathrm{cd}}(\tau_3+\tau_2+\tau_1)\bar{\mu}_{\mathrm{bc}}(\tau_2+\tau_1)\bar{\mu}_{\mathrm{ab}}(\tau_1)\bar{\mu}_{\mathrm{da}}(0)\mathrm{f}_{\mathrm{abcd}}^{(-)}\right\rangle \end{aligned} \tag{3}$$

$$\begin{aligned} \mathrm{f}_{\mathrm{abcd}}^{(+)} &= \exp\left[-\mathrm{i}\int_{\tau_2+\tau_1}^{\tau_3+\tau_2+\tau_1} \omega_{\mathrm{ba}}(\tau)\,\mathrm{d}\tau - \mathrm{i}\int_{\tau_1}^{\tau_2+\tau_1} \omega_{\mathrm{ca}}(\tau)\,\mathrm{d}\tau - \mathrm{i}\int_0^{\tau_1} \omega_{\mathrm{da}}(\tau)\,\mathrm{d}\tau\right] \\ \mathrm{f}_{\mathrm{abcd}}^{(-)} &= \exp\left[-\mathrm{i}\int_{\tau_2+\tau_1}^{\tau_3+\tau_2+\tau_1} \omega_{\mathrm{dc}}(\tau)\,\mathrm{d}\tau - \mathrm{i}\int_{\tau_1}^{\tau_2+\tau_1} \omega_{\mathrm{db}}(\tau)\,\mathrm{d}\tau - \mathrm{i}\int_0^{\tau_1} \omega_{\mathrm{da}}(\tau)\,\mathrm{d}\tau\right] \end{aligned} \tag{4}$$

Further simplification of Eq. (2) requires that we neglect the dependence of the transition moment on the bath (Condon approximation) and neglect orientational factors (isotropic approximation). Then for the specific case of Gaussian dynamics one can make the cumulant approximation and truncate at second order to obtain an expression of the following form,

$$R^{(1)}(\tau) = |\mu_{ab}|^2 e^{-i\omega_{ab}\tau} \exp\left[-\int_0^{\tau}\int_0^{\tau''} \left\langle \delta\omega_{ab}(\tau'')\,\delta\omega_{ab}(\tau')\right\rangle d\tau' d\tau''\right] \tag{5}$$

where, $\delta\omega_{ab}$ is the deviation of ω_{ab} from its mean value. Response functions in the second cumulant approximation can be derived analytically for the specific form of a system bi-linearly coupled to a harmonic bath. This leads to the commonly used phenomenological models, such as the Brownian oscillator model.[1,4]

Mixed quantum-classical models apply a semi-classical approximation to Eqs. (2)–(4). This replaces the time propagator $e^{-iH_B t/\hbar}$ with classical dynamics for the bath variables *q*, and replaces the trace over the bath with an equilibrium average over phase space. For the quantum operator $\mathbf{m}(Q,q,t)$, only the system coordinate *Q* remains quantized, and the orientation and magnitude of the dipole moment and the dynamics depend on the classical degrees of freedom $\tilde{q}_\alpha$. In practice, use of this approximation in nonlinear spectroscopy has been handled in different ways, but practical considerations have dictated that $\omega_{ab}(t)$ and $\bar{\mu}_{ab}(t)$ are not separately calculated for each time step. Instead, within an adiabatic approximation, one can use a mapping that correlates these variables with the bath coordinates *q*. For instance,

$$\omega_{ab} = \omega_{ab}^{0}\left(1+\sum_{\alpha} a_{\alpha}\,\tilde{q}_{\alpha}+\cdots\right) \tag{6}$$

$$\bar{\mu}_{ab} = \bar{\mu}_{ab}^{0}\left(1+\sum_{\alpha} b_{\alpha}\,\tilde{q}_{\alpha}+\cdots\right) \tag{7}$$

Here a_α and b_α are the mapping coefficients between the bath and the transition frequency $a_\alpha = (\partial\omega_{ab}/\partial\tilde{q}_\alpha)/\omega_{ab}^0$ or transition dipole moment $b_\alpha = (\partial\bar{\mu}_{ab}/\partial\tilde{q}_\alpha)/\bar{\mu}_{ab}^0$, and ω_{ab}^0 and $\bar{\mu}_{ab}^0$ are their values in the absence of interactions with the bath. This expansion is only shown to the linear term, but the nonlinear terms in this expansion will be used where this method is most useful. The mapping may be to local or collective bath coordinates, and to as many degrees of freedom as are necessary to obtain a highly correlated single-valued mapping of $\omega_{ab}(q)$ and $\bar{\mu}_{ab}(q)$. Examples of these mappings include correlating ω_{ab} with the electric field of the bath acting on the system coordinate[8,11,21–23] and with bond length.[24,25] The construction of these maps is independent of the dynamics, and has been performed using perturbation theories for the system-bath interaction,[21,26] DFT calculations on clusters and model systems,[8,12,27,28] and empirical methods.[29] In the case of multiple interacting degrees of freedom, the site energies and couplings of the system Hamiltonian can all be constructed by mapping procedures.[30]

b. Trajectory construction

The semi-classical approximation to Eqs. (3) and (4) allows one to calculate spectroscopic observables from trajectories for the transition energy gap $\omega_{ab}(t)$ and the transition dipole moment $\bar{\mu}_{ab}(t)$. If one can obtain trajectories for the dynamics of the system, this approach provides a clear physical interpretation to the spectrum. However, added complexity exists if these must be obtained by performing molecular dynamics simulations, which introduces more difficulties in the analysis of data. Instead, we propose that classical trajectories with specified dynamical characteristics for one or more stochastic variables of the bath be constructed and used with mapping to the spectroscopic quantities to calculate or fit the experimental observables using the semi-classical approximation.

To illustrate this method, we make use of two approaches of constructing trajectories in the internal stochastic variable of the bath q to which we attribute the dynamics. In the first method, illustrated in Fig. 1, the phenomenological inputs are an equilibrium distribution function for q, $P(q)$, and a correlation function for the stochastic variable $c_q(t)=\langle q(t)q(0)\rangle$. A trajectory is generated by convoluting a vector of random values for q, $v(i)$, chosen randomly from $P(q)$, with the correlation function. A specified $c_q(t)$ is also saved in discrete form in a vector of equal length, where a time spacing Δt between points is understood. If we now associate the index of $v(i)$ with a time point $t_i = i\,\Delta t$, then a trajectory for q with the time-dependent properties of $c_q(t)$ can be obtained by convoluting,

$$q(t) = \int dt' c_q(t - t') v(t') . \tag{8}$$

In practice, we perform this convolution using fast Fourier transform methods. The time-ordered sequence of values for q can be translated into trajectories for the transition energy $\omega_{ab}(t)$ and transition dipole moment $\bar{\mu}_{ab}(t)$ on the basis of a mapping from q. A related approach is to use a transformation matrix that contains correlation information to convert Gaussian random fluctuations in the system-bath Hamiltonian into a correlated trajectory.[16]

The second method involves generating a trajectory by using Langevin dynamics on a potential of mean force for the stochastic variables of interest, $F(q) = -kT \ln P(q)$. The dynamics are propagated on the potential of mean force as a function of q. With trajectories for the stochastic variable $q(t)$, trajectories for the spectroscopic variables $\omega_{ab}(t)$ and $\bar{\mu}_{ab}(t)$ can be obtained using appropriate mapping.[31] Alternatively, Langevin dynamics can be run on a higher dimensional potential of mean force that explicitly accounts for the statistical relationship between $q(t)$ and $\omega_{ab}(t)$. These surfaces may have multiple minima for the purpose of describing barrier crossing kinetics.

3. Examples

To illustrate the utility and ease of the trajectory mapping method we calculate linear and nonlinear infrared vibrational spectra for three problems that are not easily addressed with existing phenomenological or analytical models. We use two approaches to trajectory construction, and provide a description of the frequency and dipole maps. With frequency and dipole trajectories in hand, we calculate the $R^{(1)}$ and $R^{(3)}$ using their semi-classical forms (Eqs. (2)–(4)). Additional details for how we calculate nonlinear and two-dimensional spectra are described in more detail in Ref. 27. In the case of 2D IR spectra, the time domain responses were windowed, zero-padded and Fourier transformed in τ_1 and τ_3 to give rephasing and non-rephasing spectra, which were summed to give 2D IR spectra.[32]

a. The Non-Condon Effect: Nonlinear IR Spectroscopy of HOD/D_2O

Ultrafast infrared spectroscopy of the OH stretch vibration has been widely used to understand hydrogen bond dynamics in liquid water.[33,34] The sensitivity of the OH stretch frequency to its local hydrogen bonding environment has made it a powerful observable to probe the evolution of the hydrogen bond network.[21,26,35] Moreover, molecular dynamics simulations using various water models, in conjunction with semi-classical approaches of calculating spectroscopy, have been extensively used to understand hydrogen bond dynamics in water.[21,35–37] Water is a highly anharmonic system and exhibits non-Gaussian dynamics, making traditional approaches to modeling the nonlinear response problematic. In particular, experiments and molecular dynamics simulations have indicated that the non-Condon variation in the transition dipole moment with OH stretch frequency is a particularly strong effect that may mask the underlying hydrogen bond dynamics in infrared spectroscopy.[29,38,39]

We used the phenomenological approach outlined above to study the non-Condon effect in nonlinear spectra of the OH stretch in HOD/D_2O. We focused on the results from three-pulse echo peak shift (PS) measurement,[40] which can measure the OH stretch frequency correlation function, giving insight into the timescales involved in HB dynamics. In their original analysis, Fecko et al.[40] fit their experimentally measured three-pulse peak shift decay to a Brownian oscillator model to extract the OH frequency correlation function.[4] This analysis accounted for finite pulse length, population relaxation, thermally-shifted ground state, and molecular reorientation.

To explore the effects of the Condon approximation on the extracted OH frequency correlation function, we fit the PS data with the trajectory mapping model that included variation of the OH transition dipole moment with OH frequency, but retained a Gaussian distribution of OH frequencies. Although evidence has indicated that water's dynamics are non-Gaussian, we chose a Gaussian distribution to illustrate the specific manner in which non-Condon behavior influences nonlinear spectroscopy. Comparison of the correlation functions that best fit the PS data with or without non-Condon corrections shows the importance of including this effect. We generated a Gaussian frequency distribution for the v = 0-1 transition centered at 3400 cm^{-1}, with its width scaled to match the full-width of the experimental linear infrared spectrum of HOD/D$_2$O. We then convoluted random frequencies within this distribution with frequency correlation functions that had the same general form as in previously published work,[40] but with varying decay timescales, and decay and oscillation amplitudes. We found the calculated spectra and PS to be very sensitive to the parameters governing the short time relaxation, and we iteratively varied the parameters of the input correlation function to find best agreement of the calculated PS with the experimental PS data. The resulting frequency trajectories were each 600 ps long, with a 6 fs time step between successive frequencies. The corresponding dipole trajectories were scaled by their non-Condon relationship to the transition frequencies,[41] as shown below:

$$\mu_{10} = 1.8336 - (1.2973\times10^{-3})\omega_{10} + (4.7136\times10^{-7})\omega_{10}^{2} - (6.8016\times10^{-11})\omega_{10}^{3} \qquad (9)$$

Here ω_{10} is specified in cm^{-1} and μ_{10} is in D. We also generated a ω_{21} distribution that was fully correlated with the ω_{10} distribution, with a fixed anharmonicity of ω_{10}-ω_{21}=180 cm^{-1}. We then calculated the third-order response from Eqs. (3) and (4) for a three-level system,[29]

$$\begin{aligned} R_{\pm}^{(3)}(\tau_1,\tau_2,\tau_3) = \mathrm{Re}\Bigg[2\Big\langle \bar{\mu}_{10}(\tau_1+\tau_2+\tau_3)\bar{\mu}_{10}(\tau_1+\tau_2)\bar{\mu}_{10}(\tau_1)\bar{\mu}_{10}(0)\ \exp\Big[\pm i\int_0^{\tau_1}\omega_{10}(\tau)d\tau + i\int_{\tau_1+\tau_2}^{\tau_1+\tau_2+\tau_3}\omega_{10}(\tau')d\tau' \Big]\Big\rangle \\ -\Big\langle \bar{\mu}_{21}(\tau_1+\tau_2+\tau_3)\bar{\mu}_{21}(\tau_1+\tau_2)\bar{\mu}_{10}(\tau_1)\bar{\mu}_{10}(0)\ \exp\Big[\pm i\int_0^{\tau_1}\omega_{10}(\tau)d\tau + i\int_{\tau_1+\tau_2}^{\tau_1+\tau_2+\tau_3}\omega_{21}(\tau')d\tau' \Big]\Big\rangle \Bigg] \end{aligned} \tag{10}$$

For calculations of the peak shift and 2D IR spectra, we averaged response functions across three dipole and frequency trajectories for waiting times <400 fs, and across five trajectories for waiting times >400 fs. We then proceeded to calculate the peak shift decay for the various trial input correlation functions, by projecting the negative (rephasing) contribution in Eq. (10) onto the τ_1 axis and plotting the maximum of this projected three-pulse echo at different waiting times, τ_2. The normalized calculated PS that included the non-Condon behavior, which best follows the behavior of the experimentally measured PS is shown in Fig. 2. The calculated PS displays the salient features of the measured PS,[40] showing a double exponential decay with timescales of ~75 ps and 1 ps with a weak recurrence at ~130 fs. However, since real pulse envelopes are critical to obtaining absolute peak shift values and were not included in our calculations, the calculated PS shows a higher zero-time peak shift of 95 fs, as opposed to the 28 fs seen in experiments.

The general nature of the extracted correlation function – double exponential decay with a weak oscillation – is similar to the one obtained by Fecko et al. The short time decay amplitude for the non-Condon case is smaller than seen in Ref. 40. Since we did not include real pulse effects, the short time component of the correlation function shows a longer decay than the correlation function deduced in Ref. 40. The oscillation in the input correlation function calculated here is of lower amplitude compared to the correlation function from Fecko et al. Figure 2 shows the input trial correlation function, with and without the non-Condon effect, used to generate the best fit of the measured PS. The correlation function that best fits the experimental PS for the Condon case displays a larger amplitude fast time drop and a slightly larger amplitude oscillation, compared to the correlation function employed after accounting for the non-Condon effect. Skinner and co-workers calculated frequency correlation functions and peak shifts for Condon, non-Condon and cumulant cases from MD simulations of SPC/E water model, and found that the non-Condon peak shift and correlation function showed a larger amplitude fast decay and a stronger under-damped oscillation compared to the latter two scenarios.[39] We tested to see if the PS calculated using our method displayed similar behavior for the two cases and found that for a given input correlation function, we see the same trend seen by Schmidt et al. for the Condon and the non-Condon PS calculations – a larger amplitude fast drop, a stronger oscillation and a smaller zero-time value for the non-Condon PS compared to the Condon case. It appears that the absence of the Condon approximation influences the short time amplitude as well as the amplitude of the oscillation in the extracted frequency correlation function, although the qualitative behavior is the same.

Extending these calculations to 2D IR spectroscopy, Fig. 2 shows the 2D IR spectra of HOD/D_2O calculated upon convoluting the random OH frequencies in a Gaussian distribution with trial correlation functions that fit the experimental PS best for both the Condon and non-Condon cases, respectively. As expected, the 2D IR spectrum with the non-Condon effect clearly shows shifts in intensity to lower frequencies compared to the Condon 2D IR spectra, due to the enhanced transition dipole strengths at lower frequencies that characterize the non-Condon behavior. These calculations are consistent with the spectra obtained from molecular dynamics simulations.[10,29,37,39]

b. Non-Gaussian Dynamics: Spectroscopy of Strong Hydrogen Bonds

The difficulties with current efforts to model vibrational spectroscopy are in striking evidence in the study of strongly hydrogen bonding systems, such as carboxylic acid dimers,[42] N:···H-O hydrogen bonds,[43] and aqueous acids and bases.[44] Here, one must consider several factors that emerge for highly anharmonic potentials – a large non-Condon effect, the importance of direct 0-2 transitions that are typically not allowed in the weakly anharmonic case, and unusual "negative anharmonicities" where $\omega_{21} > \omega_{10}$.

In our first example, we model the spectroscopy of protons in strong hydrogen bonds between water molecules and aqueous hydroxide. The anomalously fast diffusion of protons in water, both in aqueous acids and bases, has been attributed to the Grotthuss hopping mechanism of protons from a proton donor to an acceptor.[45] In the case of hydroxide, this proton donor is the hydrogen bonded water molecule. The hydrogen bond rearrangements that facilitate the stabilization of the proton donor and acceptor molecules, as well as the nature and lifetimes of hydrated proton species that participate in its transport, are currently being investigated using ultrafast nonlinear IR spectroscopy.[27,44] Molecular dynamics simulations of these systems have the additional challenge of accounting for the breaking and formation of covalent O-H bonds during Grotthuss proton transport.

Our previous 2D IR experiments to understand proton transfer in aqueous bases were performed on dilute HOD in concentrated NaOD in D_2O solutions, by probing the evolution of the OH stretch vibrational frequency during proton transfer from HOD to OD^-.[27,44] We have also described a mixed quantum-classical cluster-based mapping model that draws from a multistate empirical valence bond (MS-EVB) MD simulation of aqueous hydroxide.[46] For every snapshot in these simulations around a successful proton transfer event, an HOD molecule in the first solvation shell of the OD^- ion, along with all water molecules within ~10 Å distance from the HOD molecule, were selected as a cluster. DFT calculations were performed on these clusters by stretching the OH bond in steps of 0.1 Å and tracing the corresponding potential energy curve.[41] As the proton moves from the donor molecule to the acceptor, the curve evolves from a Morse-like potential when the proton is localized on the donor or acceptor, to a symmetric double-well when the proton is equally shared between two molecules. The potential energy curves from these DFT calculations were fit to an 8th degree polynomial, and the discrete variable representation method was used to calculate the transition frequencies and their corresponding transition dipole moments, thus generating a mapping of these quantities to the internal coordinate for the cluster.[41] In the past, we used the EVB simulations of Martinez and coworkers[46,47] and identified a collective solvation coordinate as the internal variable and used DFT-based electronic structure calculations to map this variable onto the spectroscopic quantities.[27]

For the present example, we investigate the spectroscopy that arises from large amplitude fluctuations in the hydrogen bond length between donor and acceptor. For these purposes, the most intuitive stochastic internal variable is the differential distance of the proton from donor and acceptor oxygen atoms, $\delta = \left|\mathbf{r}_{O_a H} - \mathbf{r}_{O_d H}\right|$, since it directly reports on the position of the proton as it transfers from a water molecule to a hydroxide ion. Small δ values correspond to the case where a proton is equally shared between two molecules, leading to a symmetric double-well potential and larger δ values correspond to a localized proton and a Morse-like potential. Using the same cluster-based mapping method as described above, we also extracted the associated δ for each of the clusters and mapped these onto the corresponding ω and μ.

The variation of ω_{10} and μ_{10} with δ were fit to the following equations:

$$\omega_{10} = 2581 \cdot [\tanh(1.55\delta)]^2 + 433.9 \cdot \tanh(2\delta) + 650 \tag{11}$$

$$\mu_{10} = -2.9900061 \times 10^{-11} \omega_{10}^3 + 2.8814324 \times 10^{-7} \omega_{10}^2 - 9.8588217 \times 10^{-4} \omega_{10} + 1.7987508 \tag{12}$$

Here, ω is in cm^{-1} and μ is in Debye, and the correlation coefficients for ω_{10} vs. δ and μ_{10} vs. δ were 0.73 and -0.59, respectively. Mapping parameters for all the transition frequencies and dipole moments we used are tabulated in the Supporting Information. The mappings of four of these quantities, ω_{10}, ω_{21} and μ_{10}, μ_{21}, are shown in Fig. 3. The broad symmetric double-well potential of the shared proton species (small δ) results in a significant red-shift in the transition frequencies, an enhancement of transition dipole strength, and requires that one- and two-quantum transitions to higher vibrational states, v = 2, 3 and 4, be considered for mid-IR spectroscopy in the 1000-4000 cm^{-1} region.

For the purposes of using the trajectory mapping model, the proton transfer variable δ was used as the internal stochastic variable. We generated a Gaussian distribution in δ for different peak values ranging from $\langle\delta\rangle$ = 0.6 Å to 1.1 Å and widths ranging from σ=0.25 Å to 0.35 Å. Random values of δ within each of these distributions were then convoluted with a bi-exponential time correlation function, with timescales (amplitudes) of 200 fs (0.7) and 2 ps (0.3), to obtain a correlated $\delta(t)$ trajectory. The $\delta(t)$ trajectories we use in this example are each 2.5 ns long, sampled at a 5 fs time step. Drawing on the nonlinear mapping between δ and transition dipoles and frequencies, we deduced the instantaneous transition dipole and frequency trajectories for all relevant one-quantum and two-quantum transitions. From these trajectories we calculate the third-order response functions from Eqs. (3) and (4). Since we explicitly calculate the variation of the transition dipole with δ and ω, we rigorously include non-Condon effects in calculating spectra. In practice, these integrals are evaluated for $v = 0$ to 4, leading to 30 Feynman diagrams that include pathways that exclusively involve one- or two-quantum transitions, as well as those that involve mixed one- and two-quantum transitions, and coherence during the waiting period τ_2.

The linear IR spectrum for $\langle\delta\rangle = 0.6$ through 1.1 Å are shown in Fig. 4. We found that calculated spectra were very sensitive to the nature of the input δ distribution. At large $\langle\delta\rangle$ the spectrum is dominated by the transitions >3000 cm^{-1} that correspond to the weakly anharmonic limit. With decreasing δ, and increasing double-well character to the proton transfer potential, we see a significant enhancement of the low frequency tail and the appearance of the continuum absorption in the mid-IR as seen in infrared spectra of aqueous acids and bases. The rise of an additional peak at around 800 cm^{-1} with decreased $\langle\delta\rangle$ reflects fluctuations about the equally shared double well state ($\delta = 0$), the even valued mapping of ω with δ, and the strong increase in μ for these configurations.

2D IR spectra are shown in Fig. 4 for a waiting time of $\tau_2 = 100$ fs, for $\langle\delta\rangle = 0.7$ and 1.0 Å, and $\sigma = 0.3$ Å. These spectra show similar spectral features and trends in frequency. For large δ, spectra are centered at around $\omega_1 = 3430$ cm^{-1} and the lineshape is the expected diagonally elongated doublet of a weakly anharmonic inhomogeneous system. As the center of the δ distribution shifts to smaller values, additional low frequency transitions for configurations $\delta \approx 0$ are observed. These low frequency features near 1000 cm^{-1} display the negative anharmonicities characteristic of strongly hydrogen bonded systems like the shared proton species. Streaked cross peaks correspond to species with fast fluctuations of the proton between localized and shared configurations.

As another example, we calculated 2D IR spectra of a model applicable to molecules linked by strong hydrogen bonds, such as carboxylic acid dimers. Pump-probe and peak shift spectroscopies on strongly hydrogen bonded dimers have shown evidence for strong modulation of the high frequency OH or NH vibrations at the dimer interface by inter-dimer low-frequency (bath) modes.[42,43] We explore how varying fluctuations in these low frequency vibrations that impose different dephasing criteria on the high frequency vibrations affect the 2D IR line shapes of the high frequency mode.

We consider the v = 0, 1, and 2 states of an OH stretch vibration coupled to a low frequency mode, and vary their coupling between underdamped and overdamped limits. We chose a Gaussian frequency distribution for the v = 0-1 transition of the OH stretch vibration centered at $\langle\omega_{10}\rangle = 3400\ \mathrm{cm}^{-1}$, with a width of $\sigma = 300\ \mathrm{cm}^{-1}$. We then generate a ω_{21} distribution that is fully correlated with the ω_{10} distribution, offset in frequency by a fixed anharmonicity of $\omega_{21}-\omega_{10}=200\ \mathrm{cm}^{-1}$. The system-bath interaction is represented through the analytical expressions for the complex Brownian oscillator correlation functions given by Mukamel,[1] and the damping rate is varied to examine their effect on the calculated spectra. The frequency of the intermolecular mode was set to $\omega = 200\ \mathrm{cm}^{-1}$. For the damping rate γ, we used two values for the friction, $\gamma_{OD} = 0.1319\ \mathrm{fs}^{-1}$ ($700\ \mathrm{cm}^{-1}$) and $\gamma_{UD} = 0.0028\ \mathrm{fs}^{-1}$ ($15\ \mathrm{cm}^{-1}$) for the over-damped and under-damped scenarios, respectively, and the temperature was set to 300K. The corresponding imaginary parts of the complex correlation functions are shown in Fig. 5. The over-damped correlation function shows half an oscillation of the low frequency mode, while the under-damped correlation function shows several oscillations that ring for picoseconds.

We then convoluted the uncorrelated random OH frequencies with the two complex correlation functions to generate trajectories that are each 250 ps long, at 5 fs time steps. For each case, we calculated the third-order response function using Eqs. (4) and (5) that included both the v = 0-1 and v = 1-2 transitions and the non-Condon scaling of the dipole moment according to Eq. (9). We then proceeded to examine the effect of damping on the calculated 2D IR and linear IR spectra for this system. As seen in Fig. 5, the 2D IR spectrum of an over-damped OH stretch vibration shows a single broad peak (a doublet) centered at 3400 cm^{-1}. On the other hand, under-damped modulations of the OH stretch vibration result in a low-frequency vibronic progression on the positive and negative lobes of the OH 2D IR spectrum.

c. Chemical exchange

As the final example, we model barrier crossings in a chemical exchange experiment using a trajectory generated from a Langevin simulation on a potential of mean force.[1] With the exception of the work presented in Ref. 31, most chemical exchange models assume a separation of timescales between the dephasing dynamics of the spectroscopic transition and the slower kinetics for the reaction, leading to standard kinetic equations and explicit treatment of only one time variable in the experiment.[24,48–52] In the present example, vibrational dephasing and the two-state kinetics are intertwined. Our model is parameterized to reproduce the spectroscopy and two-state exchange kinetics between two configurations of a solute that can form either zero or one hydrogen bond to the solvent.[50,51] The hydrogen bonded complex and free molecule give rise to two distinct absorption peaks in the linear IR spectrum with different center frequencies and widths.

The exchange between species depends on a generalized reaction coordinate ξ, and the free energy is constructed to have two minima when projected onto the ξ–axis. Similarly, the distribution of transition frequencies has two peaks, reflecting the two hydrogen bonding configurations. The statistical relationship between ξ and ω is expressed through a phenomenological two-dimensional probability distribution, P(ξ,ω), or equivalently the potential of mean force $F(\xi,\omega) = -k_B T \ln P(\xi,\omega)$:

$$P(\xi,\omega) = A_b \exp\left[-\frac{(\omega-\omega_{b,0})^2}{2\sigma_{\omega,b}^2} - \frac{(\xi-\xi_{b,0})^2}{2\sigma_{\xi,b}^2} \right] + A_f \exp\left[-\frac{(\omega-\omega_{f,0})^2}{2\sigma_{\omega,f}^2} - \frac{(\xi-\xi_{f,0})^2}{2\sigma_{\xi,f}^2} \right] \tag{13}$$

Here the subscripts *b* and *f* correspond to the hydrogen-bonded and free species, respectively. In the resulting potential of mean force (PMF), A, ω_0, ξ_0 and σ are the depth of the well, free-energy minimum in frequency, free energy minimum in reaction coordinate, and width of the well for the two species. The PMF is plotted in Fig. 6. In total, there are ten adjustable parameters in the PMF which were chosen such that the barrier to dissociation was roughly $0.5k_BT$ and the change in energy for forming a hydrogen bond was roughly $0.2k_BT$, and that only a modest overall correlation existed between ξ and ω. Values for all parameters are given in the caption to Fig. 6.

The trajectory for the transition frequency is obtained by integrating the coupled Langevin equations for the ω and ξ coordinates:[53,54]

$$\frac{\partial\omega}{\partial t} = -c_\omega \frac{\partial F(\xi,\omega)}{\partial\omega} - \int_0^t K_\omega(t-s)\delta\omega(s)ds + T_\omega f_\omega(t) \tag{14}$$

$$\frac{\partial\xi}{\partial t} = -c_\xi \frac{\partial F(\xi,\omega)}{\partial\xi} - \int_0^t K_\xi(t-s)\delta\xi(s)ds + T_\xi f_\xi(t) \tag{15}$$

where, δω(t) and δξ(t) refer to the deviation from their average values. The three terms on the right side of Eqs. (14) and (15) are the mean force, the non-Markovian friction, and the random force. The constants c_i and T_i are the magnitude of the acceleration and magnitude of the random force respectively. The memory kernel, $K_i(t)$ is given by the fluctuation-dissipation theorem as being proportional to the autocorrelation of the random force: $K_\lambda(t) = \left\langle f(t) f(0) \right\rangle / \left\langle \lambda^2 \right\rangle$. The proportionality constant is given by the inverse of the mean value of the square of the variable, which is typically a decreasing function of the temperature of the system.

The random force was generated from a normal Gaussian distribution using the Box-Muller method. To make the random force more realistic, it was convolved with an exponential decay with a 2 ps time constant to give rise to a correlated force trajectory. The magnitude of the random force was chosen such that there was a barrier crossing event roughly once every 4 ps. Similarly, the proportionality constants between the autocorrelation of the random force and the memory kernel were chosen such that the dynamics were not drastically affected by this term.

The Langevin equations were solved using Euler's method using 4 fs time steps to a total length of 8.4 ns. Transitions between the free and bound states are clearly visible in the trajectories, as are the failed transitions, excursions to higher energy, and transitions which occur by taking paths that are higher in energy than the transition state. The corresponding frequency trajectory shown in Fig. 6 displays clear jumps between states. From the frequency trajectory, 2D spectra were calculated as a function of waiting time using Eqs. (3) and (4). These 2D spectra at different waiting times are shown in Fig. 7.

The calculated spectra show the same features as those observed in experiments on chemical exchange systems.[52] At short times, two diagonal peaks are observed in the 2D spectrum, and appear diagonally elongated indicating inhomogeneous broadening. Inhomogeneous broadening arises due to correlations in the random force. If an uncorrelated force is used, peaks are symmetric about the diagonal even at zero waiting time. After 5 ps, spectral diffusion is complete and the peaks are completely symmetric since the random force has almost entirely lost correlation by that time. By 500 fs, a cross peak appears above the diagonal and by 750 fs, a cross peak appears below the diagonal. These are exchange cross peaks due to the molecules that underwent a barrier crossing during the waiting time. The cross peak above the diagonal corresponds to molecules that started in the bound state but dissociated to the free state. Similarly, the cross peak below the diagonal corresponds to molecules that started in the free state and formed a complex. The fact that the dissociation cross peak appears before the formation cross peak implies that the barrier to dissociation is lower than the barrier for formation. In Fig. 7, the discrepancy between the rates of formation and dissociation is seen in the 750 fs surface where the two cross peaks have different magnitudes. The relative timescale between the appearance of the cross peaks can be changed by increasing or decreasing the activation energy for the reaction by modifying the PMF. Whereas the spectral diffusion time or how early the cross peaks appear can be adjusted by changing the magnitude of the random force or by changing the memory kernel.

4. Discussion and Conclusions

The trajectory mapping method provides a phenomenological approach to modeling nonlinear spectroscopy in cases where the Gaussian approximation and the Condon approximation are not appropriate, or in cases where there are nonlinear relationships between internal dynamical variables of the bath and the spectroscopic variables ω and μ. One sets probability distributions for one or more internal dynamical variables, describes their stochastic or deterministic evolution through trajectory construction, maps the dynamical variable onto the spectroscopic variables, and evaluates the semi-classical nonlinear response function. Experimental observables can add constraints on the inputs to this model, like the width of the frequency distribution and the relevant correlation function for a given system, thus allowing the model to be used for fitting experimental spectra and deducing the underlying dynamics of the microscopic variables.

Here we concentrated on three classes of problem: (1) fitting of data to account for non-Condon effects, (2) non-Gaussian dynamics and highly nonlinear relationships between the system and bath variables, and (3) barrier crossing and complex non-Gaussian dynamics on an arbitrary PMF. However, there are several other examples and different types of spectroscopy that can be addressed within the trajectory mapping approach. Generally speaking, the classes of problems for which we feel this method will find most use include the following:

(1) Heterogeneous dynamics: Cases in which a dynamical property of the system depends on an evolving bath coordinate can be treated with trajectory mapping. For instance an inhomogeneous system may exhibit a frequency-dependent population relaxation, which can be addressed by mapping frequency to an instantaneous relaxation rate $k_{ab}(t)$. One can integrate over this time-varying relaxation rate in the response function, i.e. $\exp(-\int k_{ba}(\tau)d\tau)$ in the case of the linear response function, Eq. (2).[55]

(2) Correlated dynamics: The dynamics for varying relaxation processes of the system can now be treated as correlated when appropriate. For instance, orientational relaxation is often treated independent of vibrational or electronic degrees of freedom. Correlated vibrational and orientational dynamics can be obtained from Langevin simulations on a PMF that represents their statistical relationship, and mapped onto spectroscopic variables.

(3) Multiple coupled vibrations: Although the examples presented here involve mapping to the dynamics of one system coordinate, an arbitrary number of coupled system

coordinates can in principle be incorporated and the dynamics calculated non-perturbatively. Using either convolution or Langevin simulations, one can construct trajectories in internal variables that influence the frequency of oscillators (site energies) and the coupling between them. These variables can then be mapped onto a time-dependent system Hamiltonian in the site basis. The resulting trajectory in the system eigenstates and dipole moments in turn can be directly evaluated or integrated to include non-adiabatic effects.[2]

The trajectory mapping method also has drawbacks, which constraints how and when it is used. Since this involves numerical integration over one or more trajectories, constructing trajectories and calculating the response functions is more taxing than other phenomenological approaches. This means that it will be most useful as an interpretive tool for testing hypotheses regarding dynamics, whereas fitting data through error minimization will be time-consuming. Also, this approach requires a map relating stochastic internal variables to spectroscopic quantities. While the non-Condon scaling of the transition dipole with frequency can be deduced empirically,[29] maps that relate microscopic quantities like bond distances or electric fields with transition dipole and frequencies require more expensive computations, either in the form of electronic structure calculations or molecular dynamics simulations or both. Moreover, dynamics in most complex systems cannot readily be attributed to one or two microscopic quantities, and therefore, it cannot substitute for classical and *ab initio* simulations. Finally, we note that trajectory mapping, as presented here, uses entirely classical descriptions of the bath, and we have ignored the action of the system on the bath or detailed balance.

The strength of the trajectory mapping approach lies in its flexibility to use a variety of inputs for stochastic quantities and mapping parameters, allowing us to directly assess their effects on the calculated spectra. This flexibility, combined with the ability to constrain the inputs to the model from a variety of spectroscopic techniques, can prove to be a powerful and inexpensive tool to understand chemical dynamics from infrared spectroscopy.

Acknowledgements

AM, ADH and LDM contributed equally to this work. We thank Ziad Ganim for suggesting the convolution approach expressed in Eq. (8). We thank Sean Roberts for providing frequencies, dipoles and δ values for hydroxide used in this work. This work was supported by a grant from the Department of Energy (DE-FG02-99ER14988). ADH would like to thank the Department of Energy Office of Science Graduate Fellowship Program (DE-AC05-06OR23100) for a Graduate Research Fellowship. KR thanks Michael Reppert for a careful reading of the manuscript.

References

[1] S. Mukamel, *Principles of Nonlinear Optical Spectroscopy* (Oxford University Press, New York, 1995).

[2] S. Mukamel and R. F. Loring, J. Opt. Soc. Am. B **3**, 595 (1986).

[3] G. R. Fleming and M. Cho, Ann. Rev. Phys. Chem. **47**, 109-134 (1996).

[4] J. Sung and R. J. Silbey, J. Chem. Phys. **115**, 9266 (2001).

[5] S. Garrett-Roe and P. Hamm, J. Chem. Phys. **130**, 164510 (2009).

[6] S. Garrett-Roe and P. Hamm, J. Chem. Phys. **128**, 104507 (2008).

[7] S. Roy, M. S. Pshenichnikov, and T. L. C. Jansen, J. Phys. Chem. B **115**, 5431-40 (2011).

[8] T. Hayashi, T. L. C. Jansen, W. Zhuang, and S. Mukamel, J. Phys. Chem. A **109**, 64-82 (2005).

[9] T. Hayashi and S. Mukamel, J. Phys. Chem. B **111**, 11032-46 (2007).

[10] B. Auer, R. Kumar, J. R. Schmidt, and J. L. Skinner, Proc. Natl. Acad. Sci. U.S.A. **104**, 14215-20 (2007).

[11] S. A. Corcelli and J. L. Skinner, J. Phys. Chem. A **109**, 6154-65 (2005).

[12] T. L. C. Jansen and J. Knoester, J. Phys. Chem. B **110**, 22910-6 (2006).

[13] J. R. Schmidt and S. A. Corcelli, J. Chem. Phys. **128**, 184504 (2008).

[14] T. L. C. Jansen, T. Hayashi, W. Zhuang, and S. Mukamel, The Journal of Chemical Physics **123**, 114504 (2005).

[15] F. Sanda and S. Mukamel, The Journal of Chemical Physics **125**, 014507 (2006).

[16] A. G. Dijkstra, T. L. C. Jansen, R. Bloem, and J. Knoester, J. Chem. Phys. **127**, 194505 (2007).

[17] T. L. C. Jansen, W. Zhuang, and S. Mukamel, J. Chem. Phys. **121**, 10577-98 (2004).

[18] A. Tokmakoff, Time-Dependent Quantum Mechanics and Spectroscopy; Massachusetts Institute of Technology, 2003-2011, pp License: Creative Commons BY, n.d.

[19] P. L. Silvestrelli, M. Bernasconi, and M. Parrinello, Chem. Phys. Lett. **277**, 478-482 (1997).

[20] F. Paesani, S. S. Xantheas, and G. A. Voth, J. Phys. Chem. B **113**, 13118-30 (2009).

[21] J. D. Eaves, A. Tokmakoff, and P. L. Geissler, J. Phys. Chem. A **109**, 9424-36 (2005).

[22] J. Wang, W. Zhuang, S. Mukamel, and R. Hochstrasser, J. Phys. Chem. B **112**, 5930-7 (2008).

[23] C. Liang, T. L. C. Jansen, and J. Knoester, J. Chem. Phys. **134**, 044502 (2011).

[24] M. Cho, Chem. Rev. **108**, 1331-1418 (2008).

[25] J. Stenger, D. Madsen, J. Dreyer, E. T. J. Nibbering, P. Hamm, and T. Elsaesser, J. Phys. Chem. A **105**, 2929-2932 (2001).

[26] K. B. Møller, R. Rey, and J. T. Hynes, J. Phys. Chem. A **108**, 1275-1289 (2004).

[27] S. T. Roberts, P. B. Petersen, K. Ramasesha, A. Tokmakoff, I. S. Ufimtsev, and T. J. Martinez, Proc. Natl. Acad. Sci. U.S.A. **106**, 15154-9 (2009).

[28] B. M. Auer and J. L. Skinner, J. Chem. Phys. **128**, 224511 (2008).

[29] J. J. Loparo, S. T. Roberts, R. A. Nicodemus, and A. Tokmakoff, Chem. Phys. **341**, 218-229 (2007).

[30] Z. Ganim, H. S. Chung, A. W. Smith, L. P. Deflores, K. C. Jones, and A. Tokmakoff, Acc. Chem. Res. **41**, 432-41 (2008).

[31] T. L. C. Jansen and J. Knoester, J. Chem. Phys. **127**, 234502 (2007).

[32] M. Khalil, N. Demirdoven, and A Tokmakoff, J. Phys. Chem. A **107**, 5258-5279 (2003).

[33] S. T. Roberts, K. Ramasesha, and A. Tokmakoff, Acc. Chem. Res. **42**, 1239-1249 (2009).

[34] H. J. Bakker and J. L. Skinner, Chem. Rev. **110**, 1498-517 (2010).

[35] C. P. Lawrence and J. L. Skinner, J. Chem. Phys. **118**, 264 (2003).

[36] C. J. Fecko, J. D. Eaves, J. J. Loparo, A. Tokmakoff, and P. L. Geissler, Science **301**, 1698-1702 (2003).

[37] J. J. Loparo, S. T. Roberts, and A. Tokmakoff, J. Chem. Phys. **125**, 194522 (2006).

[38] A. Piryatinski and J. L. Skinner, J. Phys. Chem. B **106**, 8055-8063 (2002).

[39] J. R. Schmidt, S. A. Corcelli, and J. L. Skinner, J. Chem. Phys. **123**, 044513 (2005).

[40] C. J. Fecko, J. J. Loparo, S. T. Roberts, and A. Tokmakoff, J. Chem. Phys. **122**, 54506 (2005).

[41] S. T. Roberts, Hydrogen Bond Rearrangements and the Motion of Charge Defects in Water Viewed Using Multidimensional Ultrafast Infrared Spectroscopy, Massachusetts Institute of Technology, 2009.

[42] K Heyne, N. Huse, E. T. J. Nibbering, and T. Elsaesser, Chem. Phys. Lett. **369**, 591-596 (2003).

[43] P. B. Petersen, S. T. Roberts, K. Ramasesha, D. G. Nocera, and A. Tokmakoff, J. Phys. Chem. B **112**, 13167-71 (2008).

[44] S. T. Roberts, K. Ramasesha, P. B. Petersen, A. Mandal, and A. Tokmakoff, Journal of Physical Chemistry A **115**, 3957-72 (2011).

[45] C. J. D. von Grotthuss, Ann. Chim. LVIII **54**, (1806).

[46] I. S. Ufimtsev, A. G. Kalinichev, T. J. Martinez, and R. J. Kirkpatrick, Phys. Chem. Chem. Phys. **11**, 9420-30 (2009).

[47] I. S. Ufimtsev, A. G. Kalinichev, T. J. Martinez, and R. J. Kirkpatrick, Chem. Phys. Lett. **442**, 128-133 (2007).

[48] Y. S. Kim and R. M. Hochstrasser, J. Phys. Chem. B **110**, 8531-4 (2006).

[49] Y. S. Kim and R. M. Hochstrasser, Proc. Natl. Acad. Sci. U.S.A. **102**, 11185-90 (2005).

[50] J. Zheng and M. D. Fayer, J. Phys. Chem. B **112**, 10221-7 (2008).

[51] K. Kwak, J. Zheng, H. Cang, and M. D. Fayer, J. Phys. Chem. B **110**, 19998-20013 (2006).

[52] K. Kwac, C. Lee, Y. Jung, J. Han, K. Kwak, J. Zheng, M. D. Fayer, and M. Cho, J. Chem. Phys. **125**, 244508 (2006).

[53] J. -P. Hansen and I. R. McDonald, *Theory of Simple Liquids*, 3rd ed. (Academic Press, 2008).

[54] M. Tuckerman and B. J. Berne, J. Chem. Phys. **98**, 7301 (1993).

[55] Y.-S. Lin, P. A. Pieniazek, M. Yang, and J. L. Skinner, J. Chem. Phys. **132**, 174505 (2010).

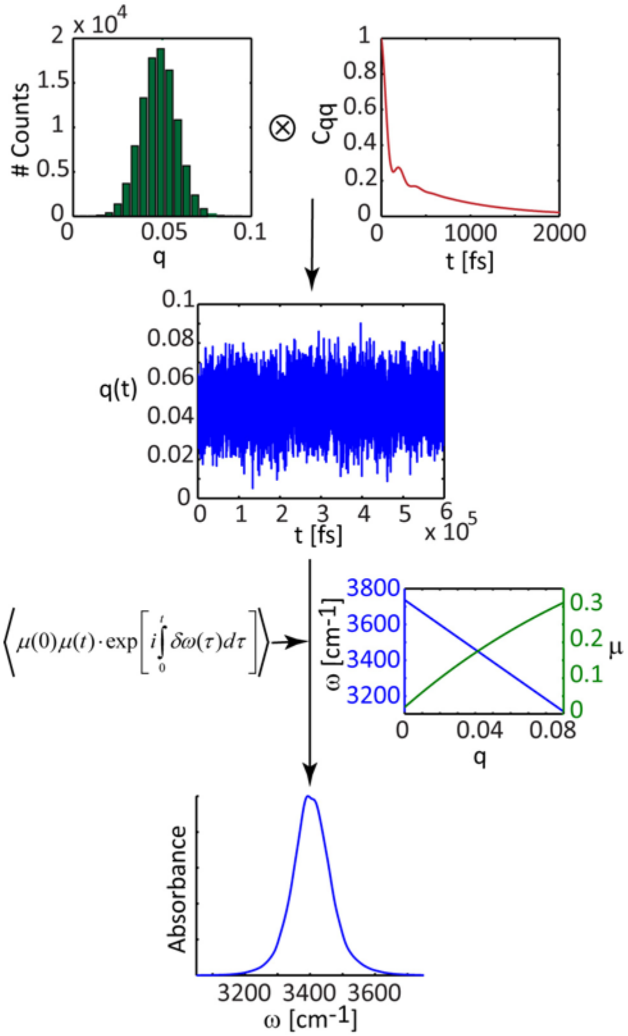

Figure 1: Procedure for calculating spectra. We identify the stochastic variable best suited for the problem, propose a random distribution for the variable and convolve it with a correlation function to arrive at the instantaneous correlated trajectory of the stochastic variable. We then generate a mapping between the variable and spectroscopic quantities like transition dipole and frequency. This mapping gives rise to a correlated frequency and transition dipole trajectory, which we use to calculate response functions and spectra. In this illustration, the stochastic variable q corresponds to the collective electric field of solvating D_2O molecule projected onto the O-H bond of an HOD molecule.

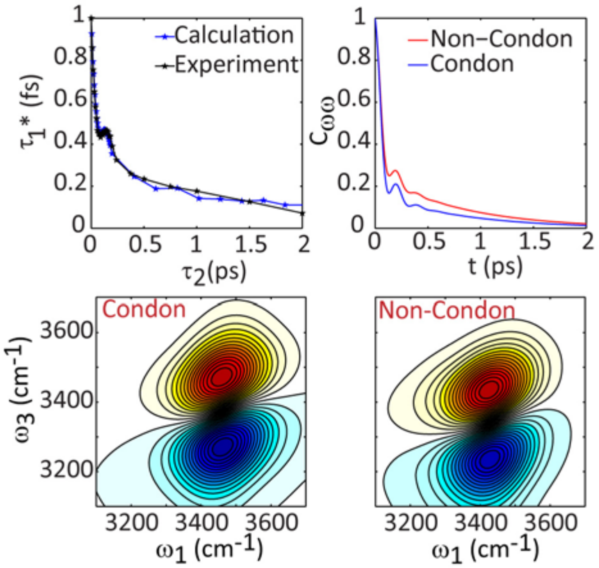

Figure 2: Comparison of the normalized three-pulse echo peak shift calculated from our model, which includes the non-Condon effect, with the normalized experimental peak shift measurement (top left) of HOD/D_2O.[40] The correlation functions that went into the peak shift calculations, which gave us the best fit with experimental results for both the Condon and non-Condon response function calculations (top right). The corresponding 2D IR spectra of HOD/D_2O with (bottom right) and without (bottom left) including the non-Condon effect.

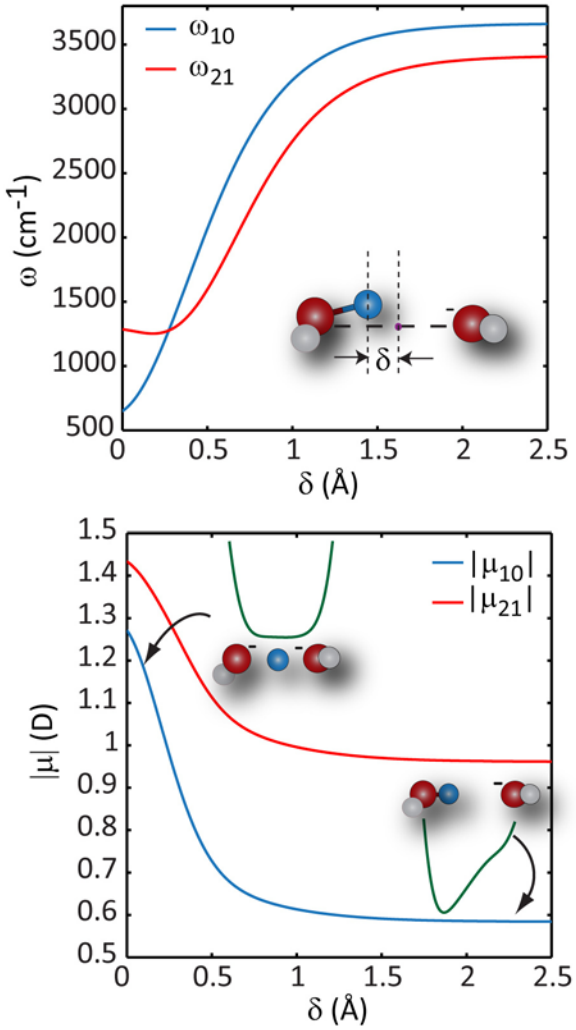

Figure 3: Mapping of the v = 0-1 and v = 1-2 OH stretch frequencies (ω_{10}, ω_{21}) to δ (top) and the mapping of the corresponding transition dipoles (μ_{10}, μ_{21}) to δ (bottom) for HOD in NaOD/D_2O. The insets in the μ vs. δ graph illustrate the potential energy curve and the position of the proton for two extreme values of δ. Equations (11) and (12) in the text show the mapping for ω_{10} and μ_{10}. Mapping parameters for the other transition frequencies and dipoles are provided in the Supporting Information. The ω_{21} and μ_{21} variables were mapped using the following expressions: $\omega_{21} = 4.8376604\times10^{-9}\,\omega_{10}^{3} + 2.7443306\times10^{-4}\,\omega_{10}^{2} + 0.44309592\omega_{10} + 1.53\times10^{3}$

and,

$$\mu_{21} = -8.5600\times 10^{-4} + 1.4429\times 10^{-7}\mu_{10} - 0.28500\mu_{10}^{2} + 0.22000\exp\left(-\left(\mu_{10} - 0.65000\right)^{2}/0.30000\right).$$

Here the ω are in units of cm^{-1} and the μ in units of D.

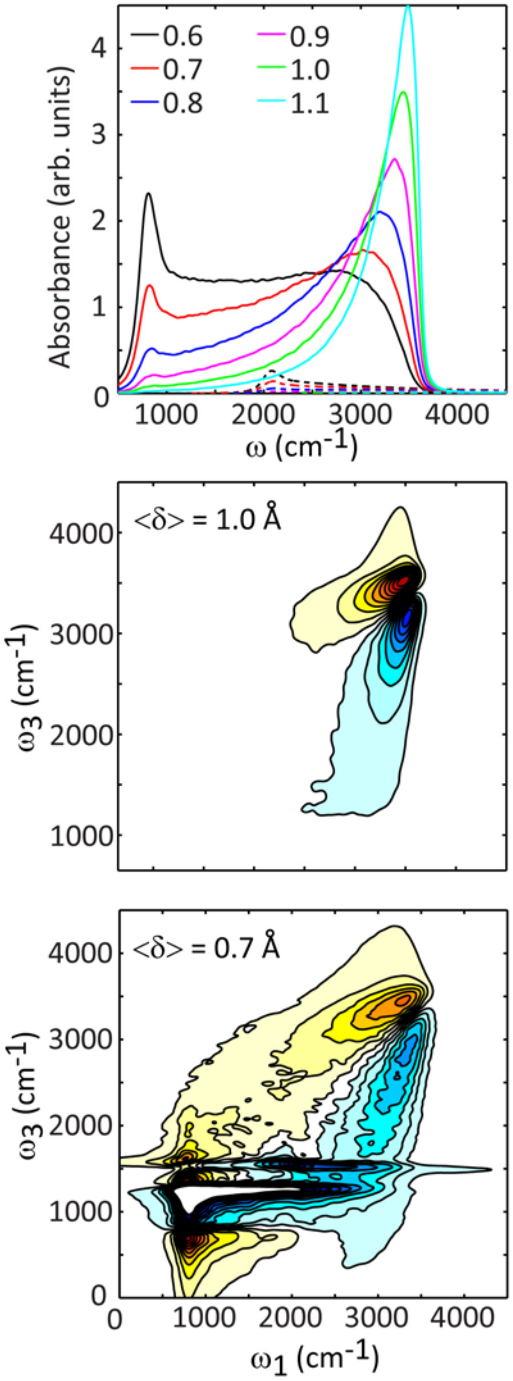

Figure 4: (Top) Linear IR spectrum of aqueous hydroxide for different values of ⟨δ⟩ (in Å), with constant distribution width of σ = 0.3 Å. Below, 2D IR spectra of hydroxide for two ⟨δ⟩ values of 0.7 Å (middle) and 1.0 Å (bottom).

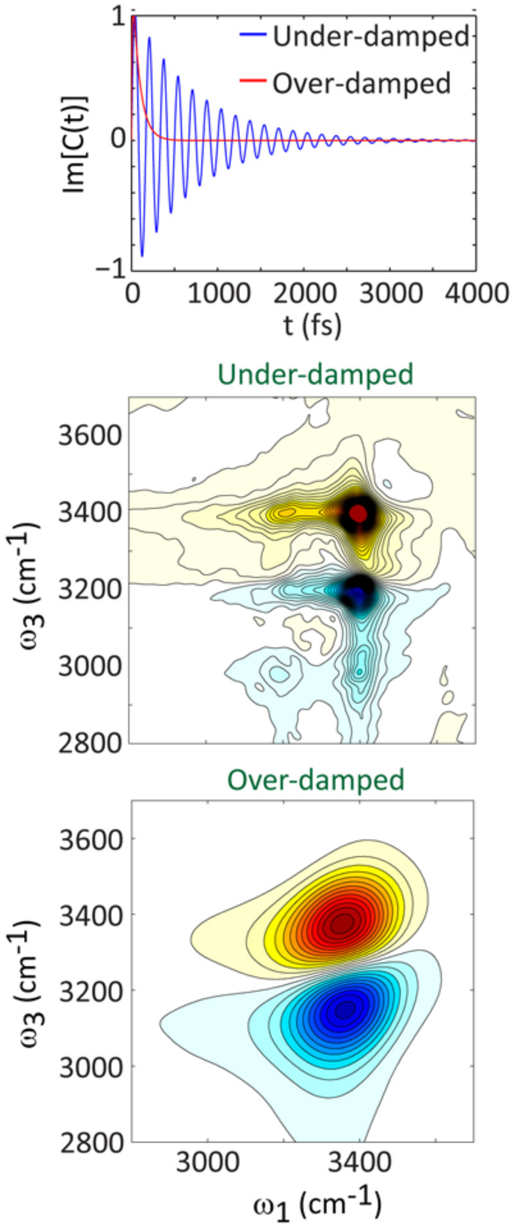

Figure 5: The imaginary part of the correlation function for the under-damped and over-damped cases for the coupling between the OH stretch vibration and the bath (top), and the corresponding 2D IR spectra (middle and bottom), respectively. The 2D IR spectrum for the under-damped case has been truncated to show the lower 75% of the contours to emphasize the low-intensity peaks.

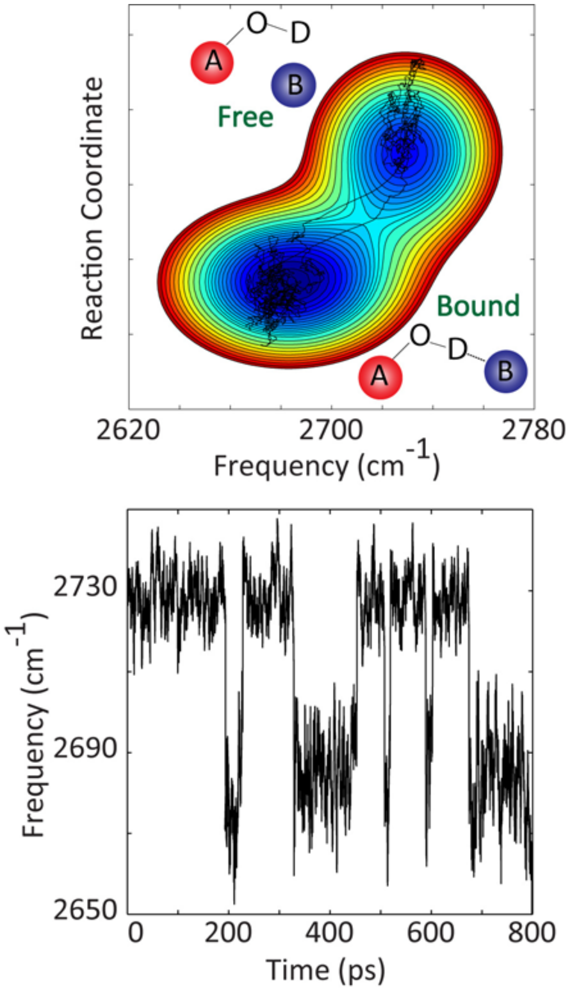

Figure 6: Potential of mean force used for the Langevin dynamics calculation of a chemical exchange process (top). The parameters used for the potential of mean force are: $\omega_{f,0}$ = 2729 cm^{-1}, $\sigma_{\omega,f}$ = 22.4 cm^{-1}, $\omega_{b,0}$ = 2683 cm^{-1}, $\sigma_{\omega,b}$ = 28.3 cm^{-1}; $\xi_{f,0}$ = 0.465, $\sigma_{\xi,f}$ = 0.0316, $\xi_{b,0}$ = 0.378, $\sigma_{\xi,b}$ = 0.0387; A_f = 0.88, A_b = 1.08. The correlated frequency trajectory showing the exchange between the free and the bound state (bottom).

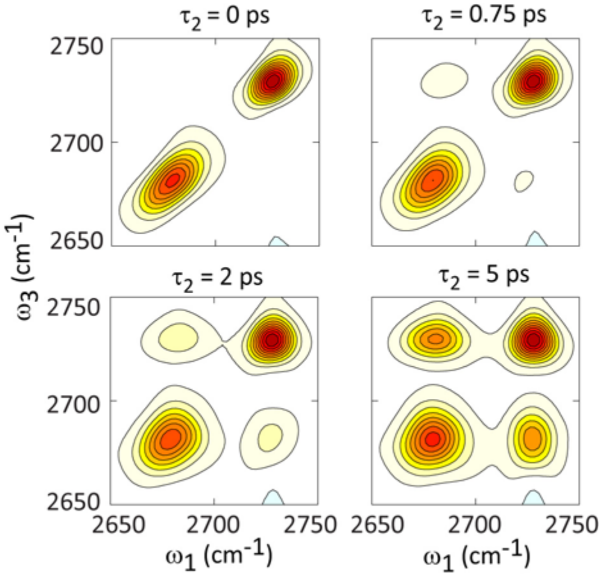

Figure 7: Waiting time series of 2D IR spectra calculated from Langevin simulations show the evolution of the diagonal peaks from being inhomogeneously broadened to being symmetric, along with the growth of the cross peaks signifying chemical exchange. The parameters used in solving the Langevin equations are: $c_\omega = 2$ cm^{-1}s^{-1}, $c_\xi = 10^{-6}$ s^{-1}, $T_\omega = 0.030$, $T_\xi = 0.000025$, and $\left\langle \lambda^{-2} \right\rangle = 3\text{x}10^{-15}$ (units of cm^{-2} in the ω-equation and unit-less in the ξ-equation).

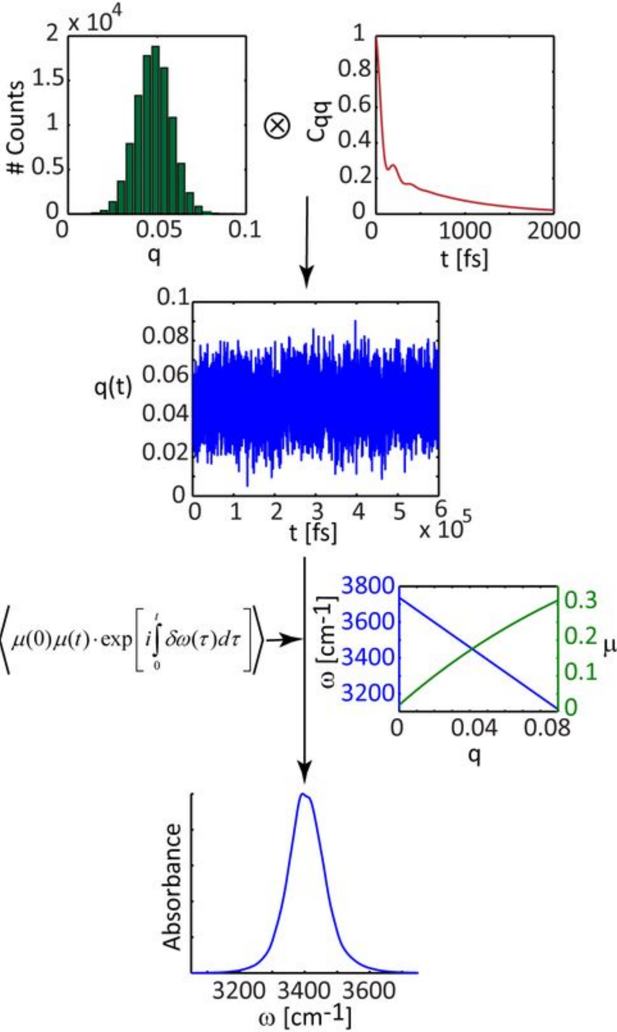

x 10^4
2
1.5
1
0.5
0
# Counts
0
0.05
0.1
q
⊗
1
0.8
0.6
0.4
0.2
0
Cqq
0
1000
2000
t [fs]
0.1
0.08
0.06
0.04
0.02
0
q(t)
0 1 2 3 4 5 6
x 10^5
t [fs]
$\left\langle \mu(0)\mu(t)\cdot\exp\left[i\int_0^t \delta\omega(\tau)d\tau\right]\right\rangle$
3800
3600
3400
3200
ω [cm-1]
0.3
0.2
0.1
0
μ
0
0.04
0.08
q
Absorbance
3200
3400
3600
ω [cm-1]

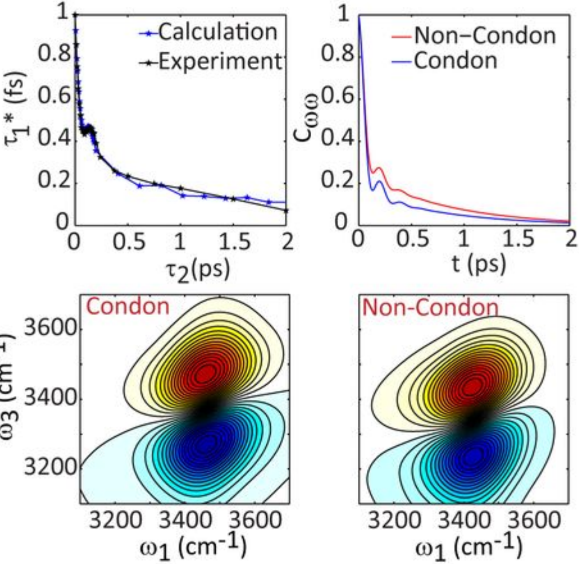
τ1* (fs)
τ2(ps)
Calculation
Experiment
1
0.8
0.6
0.4
0.2
0
0
0.5
1
1.5
2
Cωω
t (ps)
Non−Condon
Condon
Condon
Non-Condon
ω3 (cm-1)
ω1 (cm-1)
3200
3400
3600

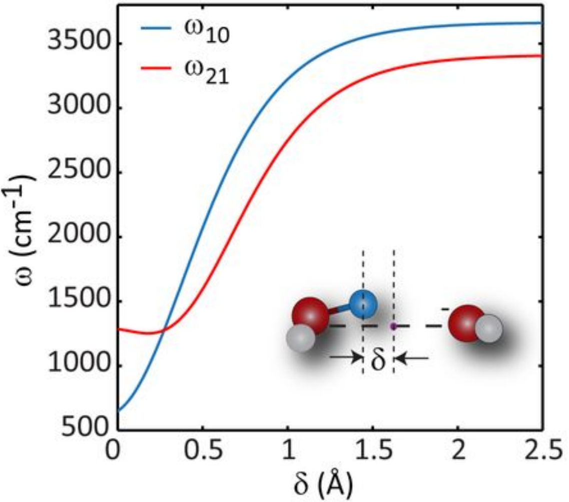

ω_{10}
ω_{21}
ω (cm^{-1})
3500
3000
2500
2000
1500
1000
500
δ
0
0.5
1
1.5
2
2.5
δ (Å)

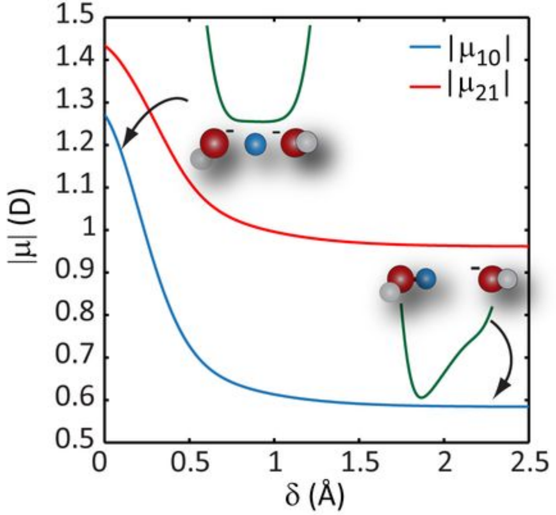

$|\mu_{10}|$
$|\mu_{21}|$
$|\mu|$ (D)
1.5
1.4
1.3
1.2
1.1
1
0.9
0.8
0.7
0.6
0.5
0
0.5
1
1.5
2
2.5
δ (Å)

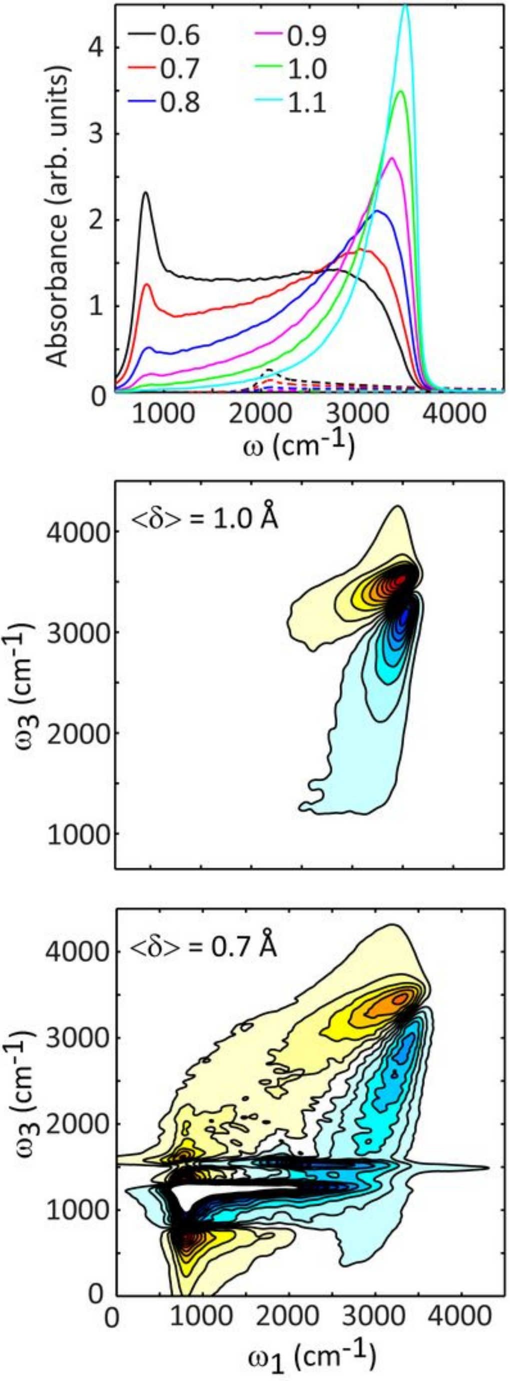
0.6
0.7
0.8
0.9
1.0
1.1
Absorbance (arb. units)
0
1
2
3
4
1000
2000
3000
4000
ω (cm-1)
<δ> = 1.0 Å
ω_3 (cm-1)
4000
3000
2000
1000
<δ> = 0.7 Å
ω_3 (cm-1)
4000
3000
2000
1000
0
0
1000
2000
3000
4000
ω_1 (cm-1)

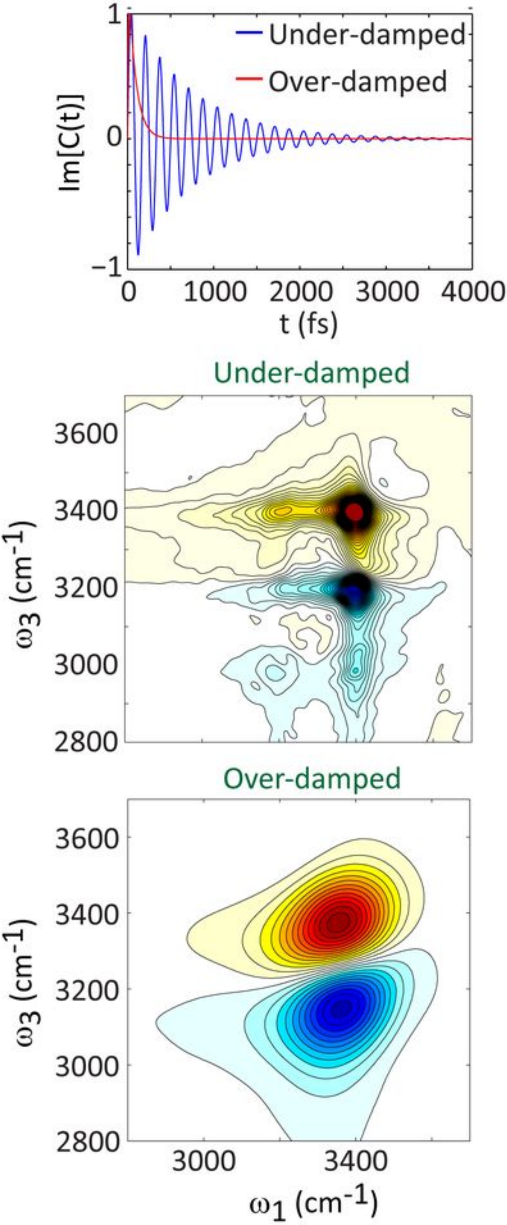

Under-damped
Over-damped
Im[C(t)]
1
0
−1
0
1000
2000
3000
4000
t (fs)
Under-damped
3600
3400
3200
3000
2800
ω_3 (cm^{-1})
Over-damped
3600
3400
3200
3000
2800
ω_3 (cm^{-1})
3000
3400
ω_1 (cm^{-1})

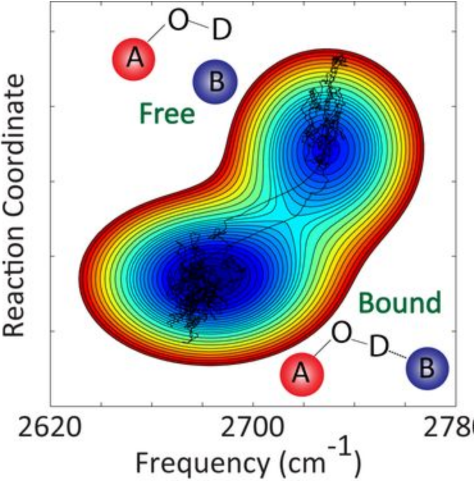
O
D
A
B
Free
Bound
A
O
D
B
Reaction Coordinate
2620
2700
2780
Frequency (cm^{-1})

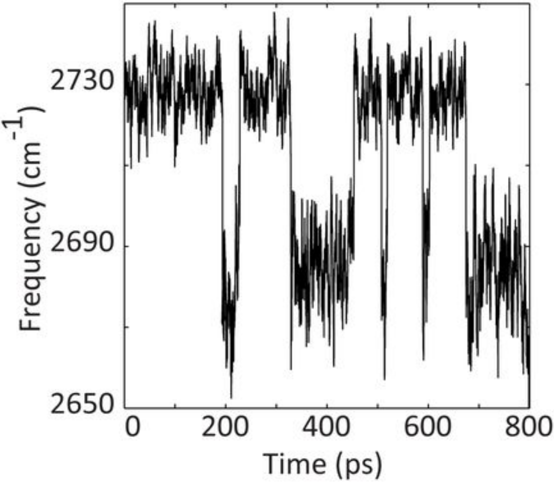
2730
2690
2650
Frequency (cm^{-1})
0
200
400
600
800
Time (ps)

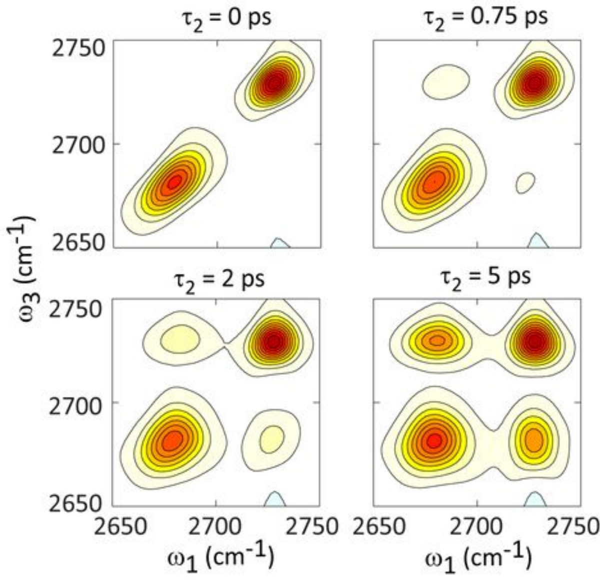
τ_2 = 0 ps
τ_2 = 0.75 ps
τ_2 = 2 ps
τ_2 = 5 ps
ω_3 (cm^{-1})
2750
2700
2650
2750
2700
2650
2650
2700
2750
2650
2700
2750
ω_1 (cm^{-1})
ω_1 (cm^{-1})

Supporting Information

A phenomenological approach to modeling chemical dynamics in nonlinear and two-dimensional spectroscopy

Krupa Ramasesha, Luigi De Marco, Andrew D. Horning, Aritra Mandal and Andrei Tokmakoff*

Department of Chemistry, Massachusetts Institute of Technology, Cambridge, MA 02139 USA

1S. Mapping parameters for transition frequencies and transition dipole moments for the OH stretch vibration of HOD in NaOD/D_2O

i	a	b	c	d
2	4.8376604×10^{-9}	2.7443306×10^{-4}	4.4309592×10^{-1}	1.530122×10^{3}
3	1.9737251×10^{-7}	$-5.7413614 \times 10^{-4}$	1.5190747	2.7048961×10^{3}
4	5.3636842×10^{-7}	$-2.4078763 \times 10^{-3}$	4.5570545	3.286824×10^{3}

Table S1: Mapping coefficients for multi-quantum transition frequencies as a function of the ω_{10} frequency: $\omega_{i0} = a_i\omega_{10}^3 + b_i\omega_{10}^2 + c_i\omega_{10} + d_i$. The ω_{i0} are in cm^{-1}.

i	a	b	c	d
1	$-2.9900061 \times 10^{-11}$	2.8814324×10^{-7}	$-9.8588217 \times 10^{-4}$	1.7987508
2	$-4.3394628 \times 10^{-12}$	7.4305822×10^{-8}	-4.414651×10^{-4}	1.0202681

Table S2: Mapping coefficients for the transition dipole moments as a function of ω_{10}: $\mu_{i0} = a_i\omega_{10}^3 + b_i\omega_{10}^2 + c_i\omega_{10} + d_i$. The ω_{i0} are in cm^{-1} and μ_{i0} are in D.

	a	b	c	A_g	x_g	σ	A_l	x_l	Γ
μ_{21}	-8.56×10^{-4}	1.4429	-0.285	0.22	0.65	0.15	0	0	0
μ_{31}	0	0	0	0.12472	0.57474	0.20513	1.4274×10^{-2}	0.47734	0.15178
μ_{32}	-1.372×10^{-3}	1.7933	-0.475	0.25	0.59	0.15	0	0	0
μ_{42}	-6.013×10^{-2}	0	0	0.15808	0.53661	0.37703	1.3649×10^{-2}	0.40965	0.11723

Table S3: Mapping coefficients for the transition dipole moments as a function of μ_{10}:

$$\mu_{\mathrm{ij}} = a + b\mu_{10} + c\mu_{10}^2 + A_g \exp\left(\frac{-(\mu_{10} - x_g)^2}{2\sigma^2}\right) + A_l \cdot \frac{\Gamma}{2} \cdot \frac{1}{\left((\mu_{10} - x_l)^2 - \left(\frac{\Gamma}{2}\right)^2\right)}.$$

The μ_{ij} are in D.